A novel environment-adaptive dual-light image enhancement framework for marine oil spill detection

Accepted for publication in Marine Pollution Bulletin.

A novel environment-adaptive dual-light image enhancement framework for marine oil spill detection

Yuqing Chen [a], Shitong Zhou [a], Wei Yu [a], Huosheng Hu [b]

[a] *Department of Automation, College of Marine Electrical Engineering, Dalian Maritime University, Dalian, China*
[b] *School of Computer Science and Electronic Engineering, University of Essex, Colchester, United Kingdom*

ABSTRACT

Ocean oil spills pose a severe threat to the marine environment. This research addresses the significant challenge of detecting low-contrast oil spills on the sea surface, a problem exacerbated by the presence of specular re-flections from sunlight in visible light images and thermal noise in infrared images. A novel environment- adaptive dual-light image enhancement framework is proposed for marine oil spill detection. Firstly, an improved Criminisi sun glint inpainting algorithm is proposed to eliminate the effects of sun glint regions in visible light images. As the oil spill regions in infrared images can be distorted by thermal noise and background interference, a novel Difference of Gaussian Weighted Guided Image Filtering (DoGWGIF) enhancement algo-rithm is then created to enhance local detail clarity and significantly increase the overall contrast of the oil spill targets, thereby improving the oil spill detection ability in the infrared images. The proposed algorithms were validated through experiments conducted on marine sun glint regions and low-contrast infrared areas, demon-strating their effectiveness. The performance index MIoU went up 1.64 % and 0.54 % for visible light images and infrared images, respectively.

Keywords:
Marine oil spill detection Dual-light images Improved Criminisi algorithm Infrared images

1. Introduction

Frequent occurrences of marine oil spill incidents have been reported. Common causes of oil spills include tanker sinkings or collisions, leakage from transportation pipelines, and local oil and gas production. For instance, a collision occurred between a tanker and a dock oil pipeline during berthing in Yeosu, South Korea, resulted in a breach of the pipeline and the spillage of 164 tons of crude oil in 2014. The surrounding maritime environments were severely impacted by the incident, significantly influencing the economic activities and social stability of adjacent coastal regions (Moon and Yun, 2016).

The impact of oil spill incidents was not limited to environmental harm but also resulted in severe economic losses in related economic sectors. Oil spills can lead to the degradation of marine and coastal ecosystems, affecting vital habitats such as coral reefs, sea grasses, and mangroves. Additionally, human resources, including coastal resorts and infrastructure, are highly sensitive to oil pollution, which can result in long-lasting economic repercussions. The overall marine pollution caused by oil spills disrupts the balance of marine life, posing risks to food security and community livelihoods (Abou Samra et al., 2020).

The impacts of oil spills on coastal areas are largely determined by several oceanographic factors, including currents, tides, wave energy, sea surface temperature, and water depth (Abou Samra et al., 2021). For instance, it has been observed that low temperatures tend to increase the viscosity of oil, making dispersion more difficult, while high temperatures are known to facilitate oil spread. Furthermore, processes such as evaporation and the formation of emulsions can significantly affect the persistence of oil in marine environments.

Consequently, the paramount importance of developing advanced monitoring technologies for the detection of marine oil spills was highlighted. Currently, many oil spill detection methods have been developed based on traditional Machine Learning (ML) and those based on deep learning.

Traditional ML approaches can hold significant promise in detecting oil spills. For example, hyperspectral data at different solar times were analyzed, and oil type identification experiments were conducted using both full spectrum and selected characteristic bands with the Support Vector Machines (SVM) model (Yang et al., 2020). It was found that the accuracy of oil type identification was improved when selected characteristic bands were used compared to the full spectrum. Reflectance data was coupled with ML technologies to detect oil presence in terrestrial satellite imagery and models for estimating concentrations using data of various oil concentrations (Trujillo-Acatitla et al., 2022). The SVM based Synthetic Aperture Radar (SAR) image marine oil spill semantic segmentation model was improved by training with more comprehensive feature maps to identify oil spill pixels (Wang et al., 2023). Sentinel-1 (SAR—C) and Sentinel-2 Multispectral Instrument (MSI) data were used to monitor and map oil spill incidents in the Nile Delta. The oil spill detection model in the SNAP toolbox was applied, and the importance of the Sentinel-1 sensor's Vertical-Vertical (VV) Polarization data in oil spill detection and mapping was demonstrated. Overall Accuracy (OA) and Kappa Coefficient (KC) for all classified classes, including seawater, land, and oil spills, were found to range between 86 % and 98 %, with KC values ranging from 0.73 to 0.97 % (Abou Samra and Ali, 2022). The ML models with variable complexity were developed and compared for detecting the origin, extent, and movement of large-scale oil spills, tracking the movement and potential transmission rates of the spills through ascending and descending orbits (Najafizadegan and Danesh-Yazdi, 2023). In a related study, the Random Forest (RF) algorithm was applied, resulting in an OA of 90 % to 98 % and KC values between 0.86 and 0.98 for land, water, and oil spill classes. The oil spill spread was effectively revealed through the use of decorrelation stretching and band ratios of Sentinel-2 MSI data (Abou Samra and Ali, 2024).

In the domain of deep learning-based methods, a novel Semantic Segmentation Network (SSN) designed for processing oil spills images was introduced, which can accurately identify low-contrast oil spills on the sea surface (Chen et al., 2024). The high accuracy and good real-time performance of the proposed network in oil spill detection were verified by ablation experiments. An oil film thickness inversion generative adversarial and convolutional neural network (OG-CNN) model was proposed for oil spill emergency monitoring(Jiang et al., 2020). The model consists of a self-expanding module for oil film spectral feature data and an oil film thickness inversion module. In the model stability test, excellent robustness was demonstrated. The Crude Oil Spill Background and Boundary Supervision Detection Network (CBD-Net) was proposed with boundary details enhanced through optimized edge supervision (Zhu et al., 2021). A model based on graph convolution architecture and fusion of spatial-spectral information for real oil spill detection was proposed to reduce the spectral difference between oil films and seawater (Yang et al., 2023). A fast and effective SAR-based oil spill detection method using Faster Region-based Convolutional Neural Network (R-CNN) was introduced, which significantly improves detection speed and accuracy, particularly for large-scale oil spills captured in Sentinel-1 and RADARSAT-2 SAR images (Huang et al., 2022). Additionally, a deep learning-based approach for optical remote sensing of oil spills was developed, capable of detecting and classifying weathered oils from images captured by 7 satellites with different sun glint reflection contrasts (Wang et al., 2024).

Currently, sun glint image inpainting is divided into traditional methods and deep learning methods. Significant contributions have also been made by traditional methods. A method for removing specular reflection from marine surface images captured by drones was proposed in (Wang et al., 2017). Sun glint regions in marine surface images were first identified based on intensity ratio, and then the FMM algorithm was used to quickly restore these regions, obtaining high-quality marine surface images. To address the issue of information loss in sun glint regions in real scenes, a sun glint image enhancement algorithm based on dark channel prior was proposed (Xin et al., 2021). The global illumination component was estimated using a moving window minimum filter, a weighted function based on local pixel color difference was introduced to solve image halo artifacts, and transmittance was finally optimized with an improved guided filtering algorithm to enhance computational efficiency.

On the other hand, a deep learning methodology was proposed for removing sun glint regions in endoscopic imaging based on a partial convolution network (Zhang et al., 2023a). The image was divided into sun glint and non-sun glint regions using an illumination compensation brightness threshold, and sun glint region pixels were painted with a partial attention network. A dual-mask-guided deep learning model was introduced to remove sun glint regions from industrial product surface images while preserving defect regions (Yuan et al., 2023). A rapid method for sun glint removal was introduced by leveraging the combination of U2-Net for detecting sun glint reflections and LaMa for subsequent removal through advanced image inpainting techniques (Guo et al., 2022). A groundbreaking sun glint image inpainting algorithm was introduced by devising a method for swift detection of sun glint regions through a pixel classification table within the Hue, Intensity, Saturation (HIS) color space, followed by image inpainting employing a generative multi-column CNN (Kang et al., 2021).

The application of infrared image enhancement algorithms has become increasingly widespread in military, medical, and scientific research fields. Owing to the typically low contrast inherent in infrared images, enhancement processing is crucial for improved target extraction and recognition. Presently, the methodologies for infrared image enhancement can be classified into traditional methods and deep learning methods. Traditional methods rely on edge detection and histogram equalization techniques, whereas deep learning approaches leverage deep neural networks for autonomous learning and processing.

As a traditional algorithmic approach, an enhancement algorithm was introduced to initially segregate infrared images into base and detail components via a bilateral filter (Zhang and Zhang, 2021). Subsequently, the detail component was transformed into the neutral domain employing a neutral set-based enhancement algorithm. The neutral domain was characterized by three membership functions: True, False, and Indeterminacy, correlating respectively with the image's target, background, and transitional regions. As a result, the contrast of infrared images was effectively augmented by this algorithm while detail integrity was preserved.

A multi-frame image super-resolution algorithm rooted in edge gradient regularization was proposed in (Sun et al., 2021), incorporating an edge preservation regularization term to amplify infrared image resolution and enhance the visibility of weak infrared targets. A high dynamic range infrared image enhancement technique via wavelet transform was developed (Zhang et al., 2023b), bifurcating images into low and high-frequency data. For low-frequency information, adaptive histogram equalization was utilized to bolster contrast, while high-frequency data undergo adaptive coefficient enhancement through gamma-transform determined gain coefficients, culminating in a wavelet inverse transform. A novel dual-stream deep fully convolutional neural network was unveiled (Pang et al., 2023), engineering an infrared detail enhancement subnetwork alongside a global content invariant subnetwork for the adaptive augmentation of infrared features.

Deep learning-based infrared image enhancement methods have been extensively studied. A Convolutional Neural Network (CNN) model that encompasses feature extraction and image enhancement to augment the contrast of infrared images was proposed (Zhong et al., 2023). This enhancement was particularly beneficial for target localization in automatic driving detection systems. To address the challenge of losing details and texture in low-light infrared images, a Multi-layer and Multi-scale Feature Fusion Network (MMFF-Net) was introduced (Zhu et al., 2024). The brightness of images under low-light conditions was enhanced while preserving the details consistent with the source image. A dual CNN that incorporates attention mechanisms was developed to boost the low contrast characteristic of infrared images (Gao et al., 2023). This architecture significantly improves the feature extraction capability and generates high-quality infrared images through a fusion module.

Despite significant advancements in marine oil spill detection, existing methodologies often struggle to handle the challenges posed by complex oceanic conditions such as sun glint in visible light images and low contrast in infrared images. Most previous approaches have primarily focused on detecting oil spills using individual data types without fully leveraging dual-light information, and have lacked robust preprocessing methods to address these challenges effectively. This paper addresses these gaps by introducing a novel oil spill image enhancement preprocessing method that integrates both visible and infrared image enhancement techniques. These innovations provide crucial improvements to marine oil spill monitoring systems, filling gaps in the existing research and offering more reliable and accurate detection in challenging environmental conditions:

- An enhanced version of the Criminisi inpainting algorithm is proposed for the elimination of sun glint regions in images. Initially, the priority calculation formula is modified by transitioning from a multiplication to an additional relationship between the confidence and data terms, thereby boosting the algorithm's stability and precision. Furthermore, enhancements to the best matching block formula are constructed by integrating pixel gradient and Euclidean distance information, which can improve the accuracy of matches in images characterized by complex texture patterns.
- A new infrared image enhancement method is developed, which employs weighted guided filtering technique for image layering to augment infrared imagery. The base and detail layers are separately enhanced to significantly elevate the sharpness of local details and the overall contrast of oil spill targets.

The rest of the paper is structured as follows. Section 2 presents the multi-stage image preprocessing and enhancement techniques, including an improved Criminisi sun glint inpainting algorithm for marine oil spill detection and an infrared image layer enhancement algorithm with Gaussian weighted guided image filtering. Experimental results and analysis are presented in Section 3 to demonstrate the feasibility and performance of the proposed framework. Finally, a brief conclusion and future work are given in Section 4.

2. Multi-stage image preprocessing and enhancement

When detecting oil spill images on the sea surface, the captured images often show sun glint regions because the camera captures specular reflections of sunlight. The presence of these sun glint regions not only reduces the quality of the images but also severely affects the accuracy of oil spill detection. Therefore, to eliminate the impact of sun glint regions on the detection targets, it is necessary to preprocess the images inpainting of the acquired image containing sun glint regions. To address these issues, this paper proposes an improved Criminisi sun glint inpainting algorithm, which improves both the priority model and the best matching block model. To address the deficiencies in the priority model, brightness value information is introduced into the model to enhance the priority of inpainting the boundaries of sun glint regions. For the best matching block model, the existing matching criteria are supplemented with pixel gradient and Euclidean distance information to reduce the impact of a single matching criterion on image inpainting. The improved Criminisi sun glint inpainting algorithm is used to inpainting sun glint regions in sea surface images, thereby improving the quality of oil spill images and ensuring the accuracy of subsequent detection.

Compared to visible light imaging, infrared image has unique advantages in low light and nighttime conditions, making it effective for monitoring and identifying oil spill incidents, it also faces a series of challenges. For example, it is susceptible to thermal noise and background interference, which can lead to distortion in the detail of the oil spill target region. Therefore, before using infrared images for oil spill detection, it is necessary to perform enhancement preprocessing on the infrared images to improve the quality of the infrared images. Thus, a novel Difference of Gaussian Weighted Guided Image Filtering (DoGWGIF) image layering enhancement algorithm was presented in this paper.

Remark 1. Based on the data source and acquisition process described in reference (Chen et al., 2024), this study primarily focuses on improving the Criminisi algorithm to restore solar flare regions, and enhancing infrared images using the DoGWGIF algorithm, which ensures the reliability and consistency of the data source.

2.1. Improved Criminisi sun glint inpainting algorithm

2.1.1. Determine the regions that need image inpainting

In the Criminisi algorithm, the first step is to determine the region where the image inpainting is to be performed. For this purpose, the Simple Linear Iterative Clustering (SLIC) algorithm is employed in this paper to identify the image inpainting region (Kim et al., 2013). After the super-pixel clustering is completed, the average brightness of all pixels within each super-pixel block is calculated. Using the threshold method, pixel blocks with higher brightness are selected, and regions with high brightness are identified as regions where information is missing.

The formula for calculating the average brightness of a super-pixel block is shown below:

$$M = \frac{\sum_{i=1}^{N} V_i}{N} \tag{1}$$

where V_i represents the brightness of the i-th pixel in the pixel block, and N represents the total number of pixels in the super-pixel block. In RGB images, the formula for calculating pixel brightness is:

$$V_i = 0.299 \times R_i + 0.587 \times G_i + 0.114 \times B_i \tag{2}$$

where R_i, G_i and B_i are the color values of pixel$i$in the red, green, and blue channels, respectively.

The threshold method is used to select pixel blocks with high brightness by the calculation formula:

$$Gray = \begin{cases} 255 \ , M \geq T \\ 0 \ , M < T \end{cases} \tag{3}$$

If the brightness exceeds the threshold, the super-pixel block is marked as a region to be image restored with pixels grayscale values of 255; otherwise, it is marked as background with pixels grayscale values of 0. The threshold$T$is set at 245 in the experiments, and the number of super-pixels is set to 300.

2.1.2. Priority model optimization

A new priority model has been designed in the improved Criminisi inpainting algorithm proposed in this paper, with a brightness term introduced to the original Criminisi algorithm. By integrating brightness value information, more focus can be placed on processing pixels with higher brightness values.

The priority model is optimized in this paper as follows:

$$P'(p) = \alpha C(p) + \beta (D(p) + V(p)) \tag{4}$$

where $C(p)$ is the confidence term, $D(p)$ is the data term, and $V(p)$ is the brightness information of the image at position p. The weighting factors α and β satisfy:

$$\begin{cases} 0 < \alpha, \beta < 1 \\ \alpha + \beta = 1 \end{cases} \tag{5}$$

where $\alpha = 0.3$, $\beta = 0.7$. The purpose of setting α less than β is to prioritize the inpainting of regions where structural information is more pronounced. The brightness term $V(p)$ is:

$$V(p) = 0.299 \times R_p + 0.587 \times G_p + 0.114 \times B_p \tag{6}$$

where R_p, G_p and B_p are the color values of pixel$p$in the red, green, and blue channels, respectively.

2.1.3. *Optimization of the best matching block model*

In the Criminisi algorithm, the criterion for selecting the best matching sample block is determined by calculating the sum of squared differences in color within RGB images. This method relies on the relationship between the pixels of the sample block and the target block. However, this matching criterion is not suitable for handling images with complex texture structures. Therefore, the improved Criminisi sun glint inpainting algorithm proposed in this paper designs a new matching criterion that adds pixel gradient and Euclidean distance information to the original Criminisi algorithm, thereby more comprehensively considering the multiple features of the image.

By combining pixel gradient information and the Euclidean distance between pixels, the new matching criterion makes the matching process more adaptable, especially improving the accuracy of matching in images with complex texture structures. This comprehensive approach to matching, considering multiple factors, helps to improve adaptability to the complexity of image textures and enhances the performance of the algorithm.

The formula for calculating the similarity $d'(\psi_p, \psi_q)$ between the optimized pixel blocks ψ_p and ψ_q is as follows:

$$d'(\psi_p, \psi_q) = \left[d_1(\psi_p, \psi_q) + d_2(\psi_p, \psi_q)\right] {*} e^{d_3(p,q)} \tag{7}$$

where $d_1(\psi_p, \psi_q)$ represents the sum of squared differences of color values across the three channels in an RGB image. $d_2(\psi_p, \psi_q)$, represents the gradient information between corresponding position pixels in the block to be restored and the matching block. $d_3(p, q)$, represents the Euclidean distance between the central pixel point $p\left(p_i, p_j\right)$ in the block to be restored and the central pixel point $q\left(q_i, q_j\right)$ in the matching block. Their calculation formulas are shown as follows:

$$\begin{cases} d_1(\psi_p, \psi_q) = \sum^{\substack{i=1\\m}} \sum^{\substack{j=1\\n}} \left[\left(p_{i,j}^R - q_{i,j}^R\right)^2 + \left(p_{i,j}^G - q_{i,j}^G\right)^2 + \left(p_{i,j}^B - q_{i,j}^B\right)^2\right] \\ d_2(\psi_p, \psi_q) = \sum^{\substack{i=1\\m}} \left(|\nabla \psi_{pi}| - |\nabla \psi_{qi}|\right) \\ d_3(p, q) = \sqrt{(p_i - q_\mathrm{i})^2 + \left(p_j - q_j\right)^2} \end{cases} \tag{8}$$

Thus, the best-matching block can be calculated by the formulas as follows:

$$\psi_q' = argmind'(\psi_p, \psi_q) \tag{9}$$

2.2. *DoGGIF infrared image layered enhancement algorithm*

The structure diagram of the infrared image layering enhancement algorithm based on DoGWGIF is shown in Fig. 1. Initially, the image is hierarchically processed using the DoGWGIF algorithm. The filtered image serves as the base image, primarily containing the low-frequency components of the image. Subsequently, the input infrared image is subtracted from the base image to obtain the detail image.

The Contrast Limited Adaptive Histogram Equalization (CLAHE) algorithm (Muniyappan et al., 2013) is employed to enhance the base image in this paper. Additionally, the detail image may also be affected by noise. Thus, the Non-Local Means (NLM) denoising algorithm (Buades et al., 2005) is used in this paper. By adjusting the gain k, high-frequency minor details can be accurately captured, and noise interference can be eliminated. The enhanced base and detail images are adaptively weighted and fused based on calculated weights, resulting in the final infrared image.

2.2.1. *DoGWGIF algorithm*

Guided Image Filtering (GIF) (He et al., 2012) directs the filtering process based on the features and information of the guided image, allowing the details and edge information of the image to be better retained in the output image. A local linear relationship between the guided image and the output image is assumed in guided filtering, which is defined as follows:

$$q_i = a_k I_i + b_k, \forall i \in \omega_k \tag{10}$$

where q_i is the output image, I_i is the guide image, and ω_k represents a square window centered around pixel *k*. *i* represents the pixels within window ω_k. a_k and b_k are the coefficients to be determined within this window.

A linear regression function $E(a_k, b_k)$ is required to compute a_k and b_k, so that the output image q_i approximates the input image p_i.The formula for $E(a_k, b_k)$ is shown as follows.

$$E(a_k, b_k) = \sum\nolimits_{i \in \omega_k} \left((a_k I_i + b_k - p_i)^2 + \varepsilon {a_k}^2\right) \tag{11}$$

where $(a_k I_i + b_k - p_i)^2$ is the fidelity term, ensuring that when the output image q_i approximates the input image p_i, the local linear relationship between the guided image and the output image is maintained. $\varepsilon {a_k}^2$ is the regularization term, and ε is the regularization coefficient, an important parameter of the guided filter used to prevent the coefficient a_k from becoming too large.

According to formula (11), a fixed regularization parameter ε must be set during the calculation process. Due to the varying texture differences among pixels within different windows, local texture information will not be fully utilized by a fixed regularization parameter. For regions rich in local texture information, the value of a_k tends to be larger, which requires a smaller ε. Conversely, a larger ε is needed to obtain a smaller error. Therefore, to prevent blurring caused by a large regularization parameter ε at the edges of the image, the regularization parameter ε is adaptively adjusted according to the local texture information, thereby improving the filtering effect of the guided filter.

An edge detection algorithm is adopted in this paper, utilizing the magnitude of the Difference of Gaussians (DoG) edge detection algorithm (Rafiee et al., 2013) to replace the local window variance. The definition of the edge weight factor is shown as follows:

$$z(i) = \frac{1}{N} \sum\nolimits_{i'=1}^{N} \frac{|DoG(i)| + \gamma}{|DoG(i')| + \gamma} \tag{12}$$

where $DoG(i)$ is the Difference of Gaussians edge detection operator, N is the total number of pixels in the image, γ equals $(0.001 \times L)^2$, and L represents the range of grayscale values of the infrared image. For an 8-bit infrared image,$L = 256$, and the center pixel i' needs to consider all the pixels i in the image, allowing the global information of the image to be considered during the edge detection process. $\|$ represents the operation of taking the absolute value of the amplitude in the DoG

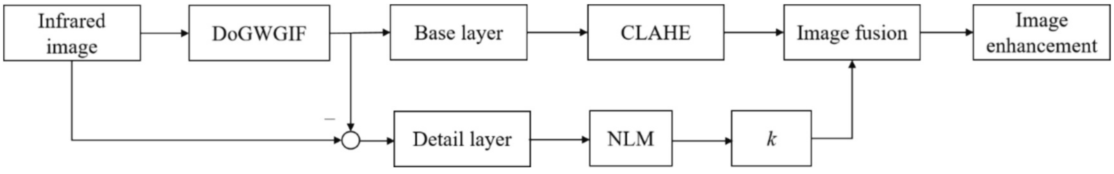

Fig. 1. Structure of DoGWGIF-based layering enhancement algorithm for infrared images.

response image, and the amplitude's magnitude represents the intensity of edges at various positions in the image.

The values of pixels at the edges are >1, while the values of pixels in smooth regions are <1. Two Gaussian filters are selected for the DoG operator in this paper, with sizes of and variances of 4 and 2, respectively. Therefore, the linear regression function $E(a_k, b_k)$ in formula (11) can be written as:

$$E(a_k, b_k) = \sum_{i \in \omega_k} \left((a_k I_i + b_k - p_i)^2 + \frac{\varepsilon}{z(i)} {a_k}^2 \right) \tag{13}$$

2.2.2. Base enhancement algorithm

To further enhance the overall brightness and visual effect of the base image, the CLAHE algorithm is used to enhance the base image in this paper. Compared to traditional HE, the image is divided into multiple small blocks for histogram equalization by CLAHE, and a contrast limit factor is introduced to control the intensity of the equalization, thus avoiding over-enhancement, and maintaining the visibility of details. Additionally, the algorithm interpolates between blocks, resulting in a smoother and more continuous image after enhancement.

To obtain a higher quality infrared oil spill image, the base image obtained through the DoGWGIF algorithm can be enhanced using CLAHE. This helps improve the overall visual quality of the image while avoiding excessive contrast enhancement in local regions.

2.2.3. Enhancement algorithm for detail layer

Although local detail information can be presented by the detail image obtained through the DoGWGIF algorithm, noise interference can also affect it. To effectively reduce the impact of this noise interference on image quality, the NLM denoising algorithm is used for processing in this paper. The basic principle of the NLM algorithm is that the entire image is searched to find regions like the pixel block, and then the target pixel is obtained through the weighted average of the pixels in the similar regions. The global information in the image is utilized by this method, rather than relying solely on the local neighborhood, thus the structure and details of the image are better preserved.

For pixels i in the detail image containing noise, the following relationship holds:

$$NLM(i) = \sum_{p \in B(i,r)} \omega(i,j) f(j) \tag{14}$$

where $NLM(i)$ is the grayscale value of pixel i after denoising, $f(j)$ is the grayscale value of the noisy pixel j, $B(i, r)$ is the square region centered at pixel i with a side length of r, and $\omega(i, j)$ is the weight between pixels i and j within the square region.

The expression of the detail layer enhancement algorithm is as follows:

$$I_d' = k \times NLM(I_d) \tag{15}$$

where k represents gain, enhancing details such as edges. I_d is the detail layer image. Experimental evidence shows that the best enhancement effect is achieved when $k = 4$.

2.2.4. Image fusion

Image fusion is the process of combining multiple images or various parts of images into a single image to display richer and more accurate information. The enhanced base and detail layer images, obtained after image layering, are fused using an adaptive linear weighting method in this paper. The specific expression is shown as follows:

$$I_{out} = \alpha I_b' + \beta I_d' \tag{16}$$

$$\begin{cases} \alpha = \dfrac{SSIM_{I_b',I}}{SSIM_{I_b',I} + SSIM_{I_d',I}} \\ \beta = \dfrac{SSIM_{I_d',I}}{SSIM_{I_b',I} + SSIM_{I_d',I}} \end{cases} \tag{17}$$

where I_{out} is the enhanced infrared image after fusion. α and β are the fusion coefficients representing the proportions of the enhanced base layer and detail layer in the fused image, respectively. Images with higher structural similarity are assigned higher weight, while images with lower structural similarity are assigned lower weight. I_b' is the enhanced base layer image, and I_d' is the enhanced detail layer image.

The entire monitoring workflow of the marine oil spill detection system is illustrated in Fig. 2.

The collected oil spill image data is initially subjected to illuminance measurement. If the illuminance is below 0.3 lx, the DoGWGIF algorithm is employed to enhance the infrared image; if the illuminance exceeds 35,000 lx, the improved Criminisi sun glint inpainting algorithm is applied to mitigate glare. Images processed through these algorithms and those within the normal illuminance range of 0.3 lx to 35,000 lx are subsequently analyzed using the ODG-ATADNet detection algorithm, proposed in our previous work (Chen et al., 2024). This adaptive workflow enables effective oil spill detection under varying illuminance conditions, ultimately providing reliable detection results.

3. Experiments and analysis

3.1. Marine image sun glint removal experiment

In section 2.1.1, the process of determining the region to be restored is explained, the super-pixel clustering and high light regions are illustrated in Fig. 3.

Following the initial experiments, comparative experiments on marine sun glint regions removal were conducted using the methods from Location-aware (Dong et al., 2021) the CDD model (Chan and Shen, 2001), the Criminisi algorithm (Criminisi et al., 2004), and the improved Criminisi algorithm, to demonstrate the effectiveness of the proposed algorithm in this paper. As shown in Fig. 4, the oil spill images under different sun glint scenarios were restored using the method from Location-aware and the CDD model. It was found that the images were still significantly affected by large sun glint regions, and the restoration results were not satisfactory.

Although the brightness in the center of the sun glint regions can be reduced by the Criminisi algorithm, the color difference between the center and the surrounding unrestored regions is substantial, and halo phenomena appear around the edges. Thus, the expectations were not fully met. The improved Criminisi algorithm visually better meets the needs for sun glint regions restoration, significantly improving the restoration quality. Subjective evaluations prove that the algorithm proposed in this paper is effective. The halo effect around the restored regions can be effectively eliminated by the proposed algorithm, achieving better visual integration of the restored regions with the surrounding environment.

Tables 1 and 2 show the PSNR and SSIM performance comparison for sun glint regions removal in marine oil spill images. Across four different sun glint scenarios, our improved Criminisi algorithm outperforms the Location-aware method, the CDD model, and the original Criminisi algorithm in both PSNR and SSIM metrics. Objective evaluations demonstrate that the proposed algorithm exhibits excellent performance.

3.2. Infrared image enhancement comparative experiment and performance analysis

The layering results of the DoGWGIF image are shown in Fig. 5. In

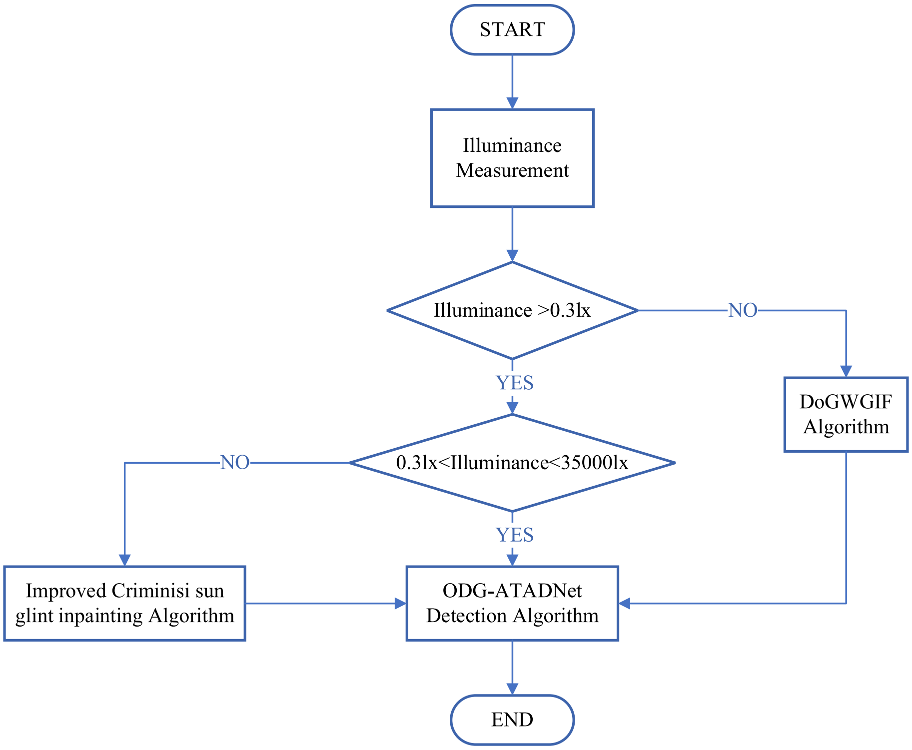

Fig. 2. Flow chart of monitoring for sea surface oil spill.

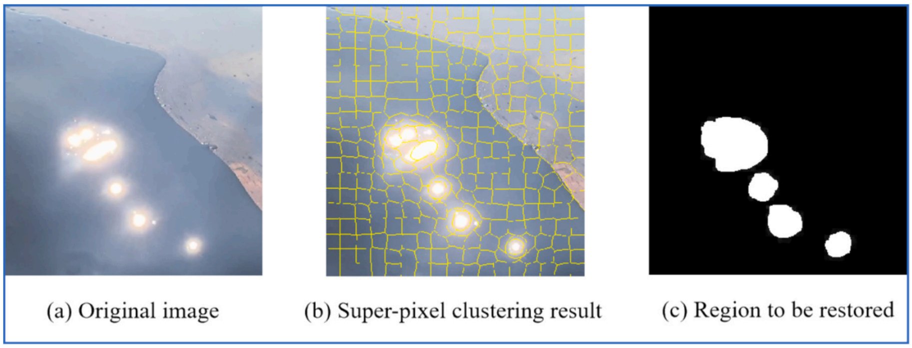
(a) Original image (b) Super-pixel clustering result (c) Region to be restored

Fig. 3. Identification of regions to be rehabilitated.

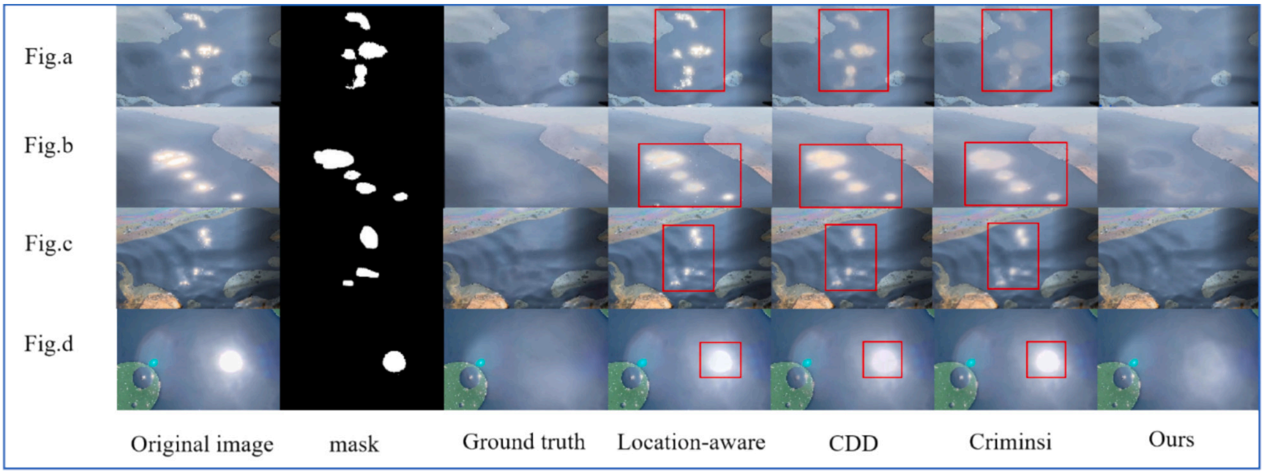

Fig. 4. Comparative experiment on sun glint inpainting of oil spill images on the sea surface.

Table 1
Comparison of PSNR performance for image sun glint removal.

Image	Location-aware	CDD	Criminisi	Ours
Fig.a	24.179	26.542	27.569	**29.364**
Fig.b	24.030	24.321	24.953	**26.398**
Fig.c	26.396	26.309	26.901	**29.502**
Fig.d	18.622	19.291	19.495	**23.003**

Table 2
Comparison of SSIM performance for image sun glint removal.

Image	Location-aware	CDD	Criminisi	Ours
Fig.a	0.891	0.924	0.945	**0.957**
Fig.b	0.910	0.915	0.922	**0.931**
Fig.c	0.882	0.902	0.909	**0.943**
Fig.d	0.859	0.860	0.865	**0.887**

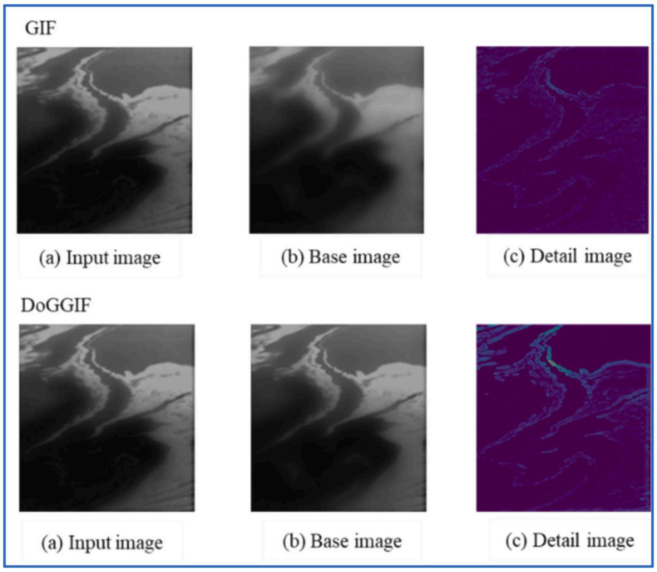

Fig. 5. Weighted bootstrap filter image layering results.

the infrared image, the edges of the oil spill region exhibit significant grayscale transitions. After the input image is processed by guided filtering, the output base image often exhibits halo effects at the edges, while the output detail image contains only a small amount of detail information. However, because an edge weight factor z is introduced by DoGWGIF to adaptively adjust the regularization parameter ε, no halo effect is shown at the edges in the resulting base image, and richer detail and texture information are possessed by the detail image.

The enhancement effect of the base image is shown in Fig. 6. Comparing the original image with the enhanced image, the improvement in brightness and detail can be clearly observed.

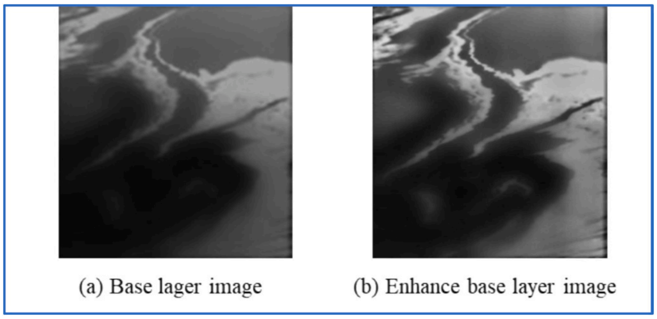

Fig. 6. CLAHE enhanced basal image.

As shown in Fig. 7, the comparison of the detail enhancement effects under different gains after NLM processing is illustrated. Although the gain can enhance details such as edges, setting it too high can lead to over-enhancement of local details. Experimental evidence shows that the best enhancement effect is achieved when $k = 4$.

The comparison of the detail enhancement effects is shown in Fig. 8. To eliminate noise interference and highlight information such as edges and textures in the detail images, the NLM algorithm and gain adjustment are employed in this paper. This approach removes noise while preserving important detailed information in the image as much as possible. From the Fig. 6, the enhanced detail images have more prominent details, sharper edges, and clearer textures, significantly improving the overall visual effect of the image.

To verify the effectiveness of the proposed infrared image enhancement algorithm, marine oil spill target infrared images were used based on weighted guided filtering image layering for experimental comparison. The proposed algorithm was compared and analyzed against the Joint Bilateral Filtering and DDE (BF&DDE) (Zuo et al., 2011) and Adaptive Histogram Partition and Brightness Correction (AHP-BC) algorithms (Wan et al., 2018).

Fig. 9 shows the comparison of infrared image enhancement effects, in which (a) is the tested infrared image, and (b), (c), and (d) are the enhancement effect images of BF&DDE, AHP-BC, and the proposed algorithm, respectively. Based on the experimental results, a subjective evaluation can be made: the BF&DDE algorithm's local detail enhancement appears blurry, failing to capture the image's minor features. Although better local detail enhancement is shown by the AHP-BC algorithm, certain exposure issues are exhibited in the overall image. In contrast, optimal effects in enhancing local details and contrast are achieved by the algorithm proposed in this paper, with the clarity of minor structures in the image successfully preserved, a more balanced overall image enhancement offered, and exposure issues avoided, thereby ensuring a natural visual effect of the image.

As shown in Table 3, the algorithm proposed in this paper outperforms the BF&DDE and AHP-BC algorithms in objective evaluation metrics such as PSNR and SSIM. The subjective evaluation mentioned above is aligned with this result, proving the effectiveness of the proposed weighted guided filtering image layering method in infrared image enhancement tasks.

3.3. *Oil spill detection algorithm and result analysis*

Before the final detection experiment, comparisons were made between various semantic segmentation algorithms, including UNet (Ronneberger et al., 2015), DeeplabV3+ (Chen et al., 2018), HRNet (Wang et al., 2020), BiSeNetV2 (Yu et al., 2021), STDC2-Seg75 (Fan et al., 2021), and ODG-ATADNet (Chen et al., 2024). Their performance in oil spill detection is summarized in Table 4, where the results demonstrate that ODG-ATADNet achieves an effective balance between accuracy and real-time capability.

In addition to quantitative performance, segmentation results from these algorithms are visualized in Fig. 10, further highlighting practical differences in their detection capabilities. As shown, varying degrees of misclassification are observed in UNet, DeeplabV3+, and BiseNetV2 for close-range oil spill detection on the sea surface. HRNet and STDC-Seg75 perform relatively well, though minor misclassifications are still present. Overall, ODG-ATADNet demonstrates exceptional performance.

The oil spill detection algorithm chosen for the designed marine oil spill monitoring system is the ODG-ATADNe algorithm in this paper, with the parameter values set during training shown in Table 5.

In oil spill images, the presence of sun glint regions often leads to missed detections in oil spill monitoring. To enhance the network's detection accuracy, the improved Criminisi inpainting algorithm is used to restore sun glint images during the training of ODG-ATADNet. The network oil spill detection results before and after the implementation of

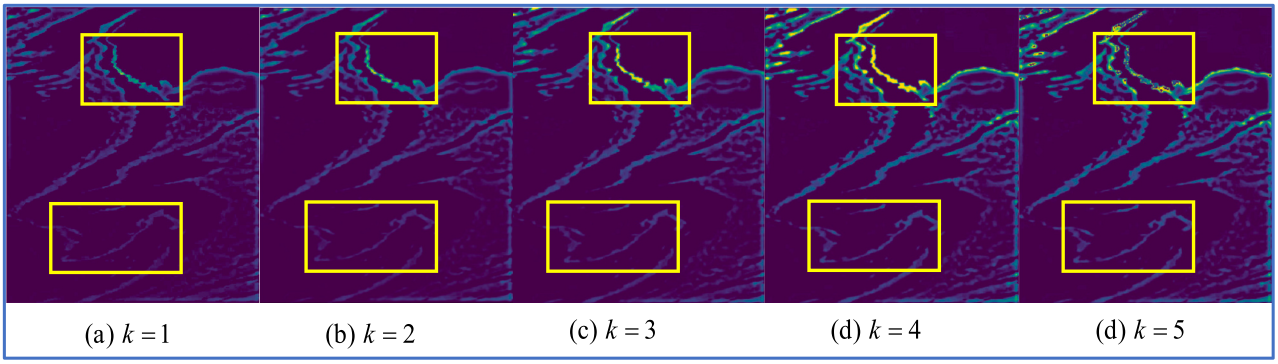
(a) $k = 1$ (b) $k = 2$ (c) $k = 3$ (d) $k = 4$ (d) $k = 5$

Fig. 7. Comparison of enhancement effect of detail section.

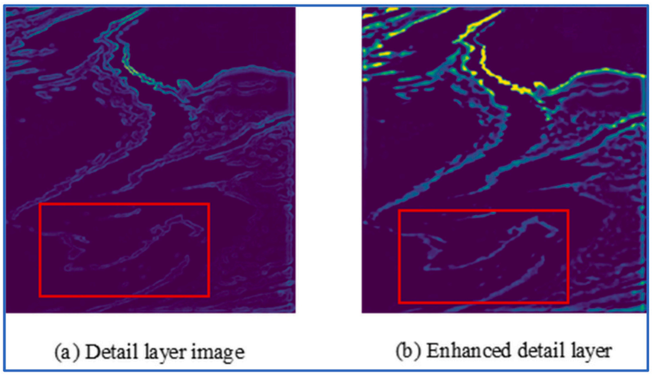
(a) Detail layer image (b) Enhanced detail layer

Fig. 8. Comparison of enhancement effect of detail section.

the improved Criminisi sun glint inpainting algorithm are shown in Fig. 11.

After the sun glint oil spill images were preprocessed using the improved Criminisi inpainting algorithm, the network's accuracy in detecting sun glint oil spill images was enhanced, reducing the occurrence of missed detections in oil spill regions. A performance comparison study on ODG-ATADNet before and after the implementation of the

Table 3
Comparison of Performance Indicators for Infrared Enhancement Algorithms.

Image	Index	BF&DDE	AHP-BC	Ours
Infrared image 1	PSNR	18.627	14.409	**20.610**
	SSIM	0.887	0.820	**0.905**
Infrared image 2	PSNR	21.598	18.427	**22.258**
	SSIM	0.731	0.727	**0.754**
Infrared image 3	PSNR	15.374	12.129	**16.181**
	SSIM	0.776	0.685	**0.783**
Infrared image 4	PSNR	16.637	13.931	**17.299**
	SSIM	0.771	0.687	**0.789**

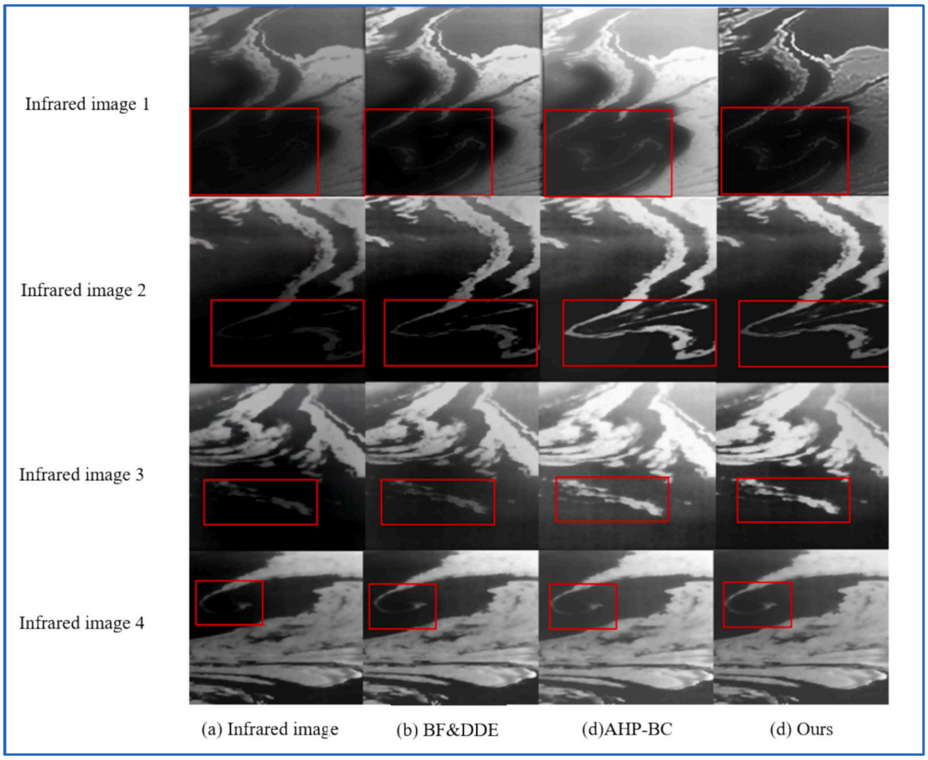

(a) Infrared image (b) BF&DDE (d)AHP-BC (d) Ours

Fig. 9. Comparison of infrared image enhancement.

Table 4
Semantic segmentation network performance comparison (The best scores at each column are shown as bold).

Method	Backbone	MPA(%)	MIOU(%)	FLOPs(G)	FPS
UNet	Vgg16	89.81	82.05	225.30	15.52
Deeplabv3+	ConvNext	93.09	86.00	40.43	23.11
HRNet	–	93.66	89.23	37.02	13.89
BiseNetV2	–	93.05	87.40	22.32	**58.45**
STDC2-Seg75	STDC2	94.45	89.45	73.27	42.84
ODG-ATADNet	GhostNetV2	**96.46**	**92.05**	**13.86**	27.45

improved Criminisi sun glint inpainting algorithm was further conducted in this paper. Table 6 shows the performance comparison of ODG-ATADNet before and after the addition of the improved Criminisi sun glint inpainting algorithm.

As shown in Table 5, during the training of ODG-ATADNet, the network's detection accuracy was improved by 1.64 % after the improved Criminisi inpainting algorithm was used to restore sun glint oil spill images. To address the issue of missed detections caused by blurred local details in infrared oil spill images, the DoGWGIF infrared image layer enhancement algorithm was employed in this paper to enhance images during the training of ODG-ATADNet. Fig. 12 shows the network oil spill detection results before and after the implementation of the DoGWGIF infrared image layer enhancement algorithm.

After the infrared images were enhanced using the DoGWGIF infrared image layer enhancement algorithm, the network's detection accuracy for infrared oil spill images was improved, reducing the occurrence of missed detections. A performance comparison study of ODG-ATADNet before and after the implementation of the DoGWGIF infrared image layer enhancement algorithm was further conducted in this paper. Table 7 shows the performance comparison of ODG-ATADNet before and after the addition of the DoGWGIF infrared image layer enhancement algorithm. During the training of ODG-ATADNet, the network's detection accuracy was improved by 0.54 % after the sun glint oil spill data was enhanced using the DoGWGIF infrared image layer enhancement algorithm.

4. Conclusion

The proposed environment-adaptive dual-light image enhancement framework can significantly improve the detection of marine oil spills by

Table 5
Parameter settings during training.

Training parameters	Parameter value
Optimizer	SGD
Momentum	0.9
Initial learning rate	0.007
Learning rate decay	Cosine Annealing
Batch size	4
epoch	500
Loss function	Focal Loss

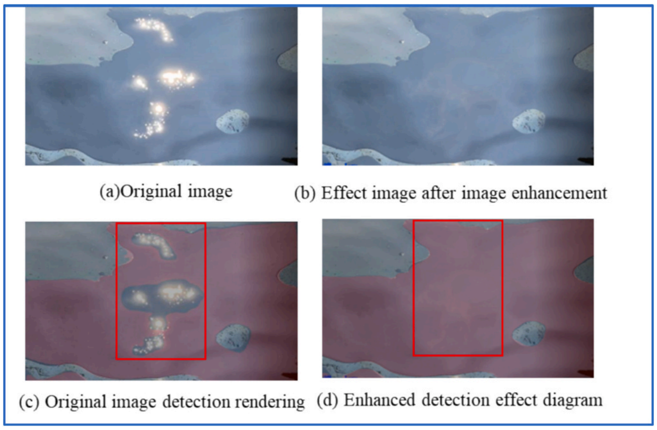
(a)Original image (b) Effect image after image enhancement
(c) Original image detection rendering (d) Enhanced detection effect diagram

Fig. 11. Comparison of the oil spill detection results before and after applying the improved Criminisi sun glint regions restoration algorithm.

Table 6
Comparison of ODG-ATADNet performance before and after adding improved Criminisi sun glint inpainting algorithm.

Network	Improved Criminisi	MIoU(%)
ODG-ATADNet		92.05
ODG-ATADNet	√	93.69

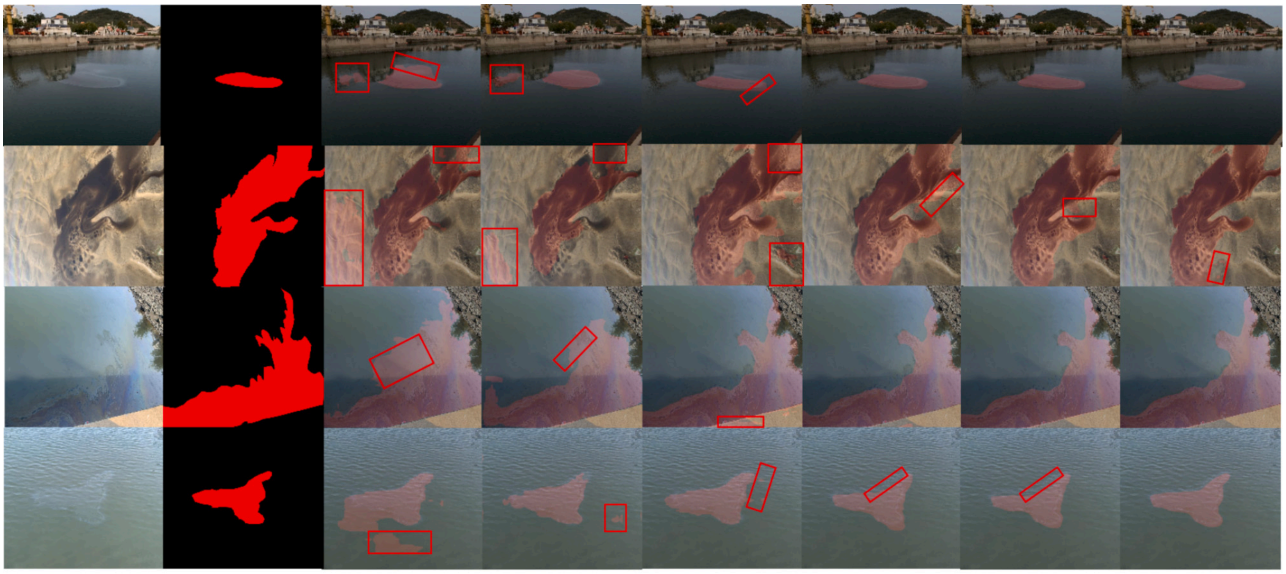
(a)Images (b)Ground Truth (c)UNet (d)DeeplabV3+ (e)BiseNetV2 (f)HRNet (g)STDC-Seg75 (h)ODG-ATADNet

Fig. 10. Semantic segmentation network performance comparison.

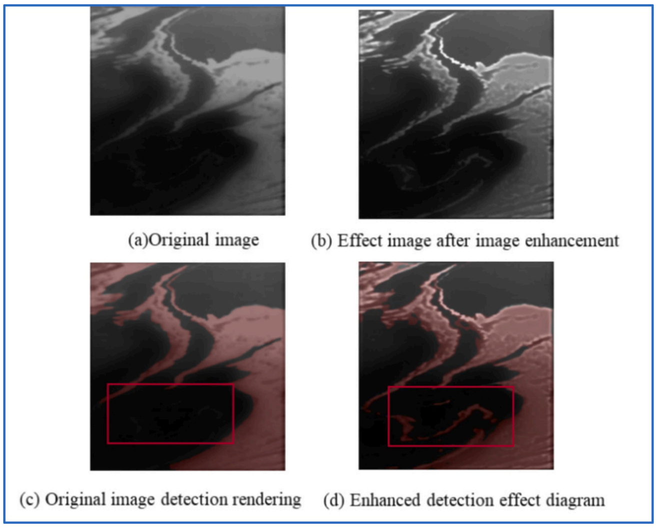

(a)Original image (b) Effect image after image enhancement

(c) Original image detection rendering (d) Enhanced detection effect diagram

Fig. 12. Comparison of the oil spill detection results before and after applying the infrared image layering enhancement algorithm.

Table 7

Comparison of ODG-ATADNet performance before and after adding DoGWGIF infrared image layering enhancement algorithm.

Network	DoGWGIF	MIoU(%)
ODG-ATADNet		92.72
ODG-ATADNet	√	93.26

addressing the specific challenges posed by sunlight reflections in visible light images and thermal noise in infrared images. By altering the priority calculation from a multiplicative to an additive relationship between the confidence term and the data term, the algorithm has achieved notable improvements in stability and precision for detecting marine oil spills. Furthermore, the method for identifying the optimal matching block has been refined by incorporating pixel gradient and Euclidean distance information, thus enhancing matching accuracy in images with intricate texture patterns. This adjustment effectively improves the quality of visible images by removing sun glint regions.

To address the issue of low contrast in infrared images, an enhancement technique leveraging a weighted guided filtering image layering algorithm has been proposed. This method improves both the base and detail layers of infrared images, enhancing the clarity of local details and increasing the overall contrast of oil spill targets.

This improvement provides a more dependable basis for subsequent detection tasks. The research offers significant advancements to marine oil spill monitoring systems. Future research can further extend this technology to other environments, such as applications in scenarios with sunlight from different angles, and it can also be applied to improve image quality in other natural settings. Moreover, this technology could be employed in fields that require enhanced detail and contrast, such as disaster monitoring (e.g., forest fires, gas leaks) or nighttime security surveillance, to further promote its development.

Nonetheless, the study recognizes existing limitations. Real-world maritime conditions, characterized by various complex factors such as waves and fog, can affect the accuracy of oil spill detection. Future research will focus on comprehensive analyses and studies of sea conditions in non-ideal environments, aiming to enhance the robustness and applicability of oil spill detection techniques in complex marine settings.

CRediT authorship contribution statement

Yuqing Chen: Supervision, Methodology, Conceptualization. **Shitong Zhou:** Writing – original draft, Validation, Methodology. **Wei Yu:** Methodology, Investigation, Data curation. **Huosheng Hu:** Writing – review & editing, Supervision.

Declaration of competing interest

This work was financially supported by the National Natural Science Foundation of China under Grant 61203082.

Data availability

The data that has been used is confidential.

References

Abou Samra, R.M., Ali, R.R., 2022. Monitoring of oil spill in the offshore zone of the Nile Delta using sentinel data. Mar. Pollut. Bull. 179, 113718. https://doi.org/10.1016/j.marpolbul.2022.113718.

Abou Samra, R.M., Ali, R.R., 2024. Tracking the behavior of an accidental oil spill and its impacts on the marine environment in the eastern Mediterranean. Mar. Pollut. Bull. 198, 115887. https://doi.org/10.1016/j.marpolbul.2023.115887.

Abou Samra, R.M., Eissa, R., El-Gammal, M., 2020. Applying the environmental sensitivity index for the assessment of the prospective oil spills along the Nile Delta coast. Egypt. Geocarto Int. 35, 589–601. https://doi.org/10.1080/10106049.2018.1533592.

Abou Samra, R.M., El-Gammal, M., Eissa, R., 2021. Oceanographic factors of oil pollution dispersion offshore the Nile Delta (Egypt) using GIS. Environ. Sci. Pollut. Res. 28, 25830–25843. https://doi.org/10.1007/s11356-021-12570-0.

Buades, A., Coll, B., Morel, J.-M., 2005. A non-local algorithm for image denoising, 2005 IEEE computer society conference on computer vision and pattern recognition (CVPR'05). IEEE, pp. 60–65. https://doi.org/10.1109/CVPR.2005.38.

Chan, T.F., Shen, J., 2001. Nontexture inpainting by curvature-driven diffusions. J. Vis. Commun. Image Represent. 12, 436–449. https://doi.org/10.1006/jvci.2001.0487.

Chen, L.-C., Zhu, Y., Papandreou, G., Schroff, F., Adam, H., 2018. Encoder-decoder with atrous separable convolution for semantic image segmentation. Proceedings of the European conference on computer vision (ECCV) 801–818. https://doi.org/10.1007/978-3-030-01234-2_49.

Chen, Y., Yu, W., Zhou, Q., Hu, H., 2024. A novel feature enhancement and semantic segmentation scheme for identifying low-contrast ocean oil spills. Mar. Pollut. Bull. 198, 115874. https://doi.org/10.1016/j.marpolbul.2023.115874.

Criminisi, A., Pérez, P., Toyama, K., 2004. Region filling and object removal by exemplar-based image inpainting. IEEE Trans. Image Process. 13, 1200–1212. https://doi.org/10.1109/TIP.2004.833105.

Dong, Z., Xu, K., Yang, Y., Bao, H., Xu, W., Lau, R.W., 2021. Location-aware single image reflection removal, Proceedings of the IEEE/CVF international conference on computer vision, pp. 5017-5026. https://doi.org/10.1109/ICCV48922.2021.00497.

Fan, M., Lai, S., Huang, J., Wei, X., Chai, Z., Luo, J., Wei, X., 2021. Rethinking bisenet for real-time semantic segmentation, Proceedings of the IEEE/CVF conference on computer vision and pattern recognition, pp. 9716-9725. https://doi.org/10.1109/CVPR46437.2021.00959.

Gao, P., Zhang, W., Wang, Z., Ma, H., Lyu, Z., 2023. A dual convolutional neural network with attention mechanism for thermal infrared image enhancement. Electronics 12, 4300. https://doi.org/10.3390/electronics12204300.

Guo, S., Wang, X., Zhou, J., Lian, Z., 2022. A fast specular highlight removal method for smooth liquor bottle surface combined with U2-net and LaMa model. Sensors 22, 9834. https://doi.org/10.3390/s22249834.

He, K., Sun, J., Tang, X., 2012. Guided image filtering. IEEE Trans. Pattern Anal. Machine Intell. 35, 1397–1409. https://doi.org/10.1109/TPAMI.2012.213.

Huang, X., Zhang, B., Perrie, W., Lu, Y., Wang, C., 2022. A novel deep learning method for marine oil spill detection from satellite synthetic aperture radar imagery. Mar. Pollut. Bull. 179, 113666. https://doi.org/10.1016/j.marpolbul.2022.113666.

Jiang, Z., Ma, Y., Yang, J., Engineering, 2020. Inversion of the thickness of crude oil film based on an OG-CNN model. J. Mar. Sci. 8, 653. https://doi.org/10.3390/jmse8090653.

Kang, H., Hwang, D., Lee, J., 2021. Specular highlight region restoration using image clustering and inpainting. J. Vis. Commun. Image Represent. 77, 103106. https://doi.org/10.1016/j.jvcir.2021.103106.

Kim, K.-S., Zhang, D., Kang, M.-C., Ko, S.-J., 2013. Improved simple linear iterative clustering superpixels, 2013 IEEE International symposium on consumer electronics (ISCE). IEEE, pp. 259-260. https://doi.org/10.1109/ISCE.2013.6570216.

Moon, J.-H., Yun, J.-H., 2016. A study on the development of regional risk mapping program for marine oil spills. J. Kor. Soc. Mar. Environ.Safety 22, 423–429. https://doi.org/10.7837/kosomes.2016.22.5.423.

Muniyappan, S., Allirani, A., Saraswathi, S., 2013. A novel approach for image enhancement by using contrast limited adaptive histogram equalization method, 2013 fourth international conference on computing, communications and networking technologies (ICCCNT). IEEE, pp. 1-6. https://doi.org/10.1109/ICCCNT.2013.6726470.

Najafizadegan, S., Danesh-Yazdi, M., 2023. Variable-complexity machine learning models for large-scale oil spill detection: the case of Persian gulf. Mar. Pollut. Bull. 195, 115459. https://doi.org/10.1016/j.marpolbul.2023.115459.

Pang, Z., Liu, G., Li, G., Gong, J., Chen, C., Yao, C., 2023. An infrared image enhancement method via content and detail two-stream deep convolutional neural network. Infrared Phys. Technol. 132, 104761. https://doi.org/10.1016/j.infrared.2023.104761.

Rafiee, G., Dlay, S.S., Woo, W.L., 2013. Region-of-interest extraction in low depth of field images using ensemble clustering and difference of Gaussian approaches. Pattern Recogn. 46, 2685–2699. https://doi.org/10.1016/j.patcog.2013.03.006.

Ronneberger, O., Fischer, P., Brox, T., 2015. U-net: convolutional networks for biomedical image segmentation, medical image computing and computer-assisted intervention–MICCAI 2015: 18th international conference, Munich, Germany, October 5-9, 2015, proceedings, part III 18. Springer, pp. 234-241. https://doi.org/10.1007/978-3-319-24574-4_28.

Sun, T., Xiong, Z., Yin, J., Wu, Y., Wang, Z., 2021. Gradient-constraint super-resolution reconstruction method serving for infrared target detection. IEEE Consum. Electron. Mag. 12, 14–25. https://doi.org/10.1109/MCE.2021.3116440.

Trujillo-Acatitla, R., Tuxpan-Vargas, J., Ovando-Vázquez, C., 2022. Oil spills: detection and concentration estimation in satellite imagery, a machine learning approach. Mar. Pollut. Bull. 184, 114132. https://doi.org/10.1016/j.marpolbul.2022.114132.

Wan, M., Gu, G., Qian, W., Ren, K., Chen, Q., Maldague, X., 2018. Infrared image enhancement using adaptive histogram partition and brightness correction. Remote Sens. 10, 682. https://doi.org/10.3390/rs10050682.

Wang, D., Liu, S., Zhang, C., Xu, M., Yang, J., Yasir, M., Wan, J., 2023. An improved semantic segmentation model based on SVM for marine oil spill detection using SAR image. Mar. Pollut. Bull. 192, 114981. https://doi.org/10.1016/j.marpolbul.2023.114981.

Wang, J., Sun, K., Cheng, T., Jiang, B., Deng, C., Zhao, Y., Liu, D., Mu, Y., Tan, M., Wang, X., 2020. Deep high-resolution representation learning for visual recognition. IEEE Trans. Pattern Anal. Machine Intell. 43, 3349–3364. https://doi.org/10.1109/TPAMI.2020.2983686.

Wang, L., Lu, Y., Wang, M., Zhao, W., Lv, H., Song, S., Wang, Y., Chen, Y., Zhan, W., Ju, W., 2024. Mapping of oil spills in China seas using optical satellite data and deep learning. J. Hazard. Mater. 480, 135809. https://doi.org/10.1016/j.jhazmat.2024.135809.

Wang, S., Yu, C., Sun, Y., Dong, J., 2017. A Specular Reflection Removal Method for Large Scale Ocean Surface Images, 2017 IEEE International Conference on Computational Science and Engineering (CSE) and IEEE International Conference on Embedded and Ubiquitous Computing (EUC). IEEE, pp. 902-907. https://doi.org/10.1109/CSE-EUC.2017.183.

Xin, Y., Jia, Z., Yang, J., Kasabov, N.K., 2021. Specular reflection image enhancement based on a dark channel prior. IEEE Photon. J. 13, 1–11. https://doi.org/10.1109/JPHOT.2021.3053906.

Yang, J., Wan, J., Ma, Y., Zhang, J., Hu, Y., 2020. Characterization analysis and identification of common marine oil spill types using hyperspectral remote sensing. Int. J. Remote Sens. 41, 7163–7185. https://doi.org/10.1080/01431161.2020.1754496.

Yang, J., Wang, J., Hu, Y., Ma, Y., Li, Z., Zhang, J., 2023. Hyperspectral marine oil spill monitoring using a dual-branch spatial–spectral fusion model. Remote Sens. 15, 4170. https://doi.org/10.3390/rs15174170.

Yu, C., Gao, C., Wang, J., Yu, G., Shen, C., Sang, N., 2021. Bisenet v2: bilateral network with guided aggregation for real-time semantic segmentation. Int. J. Comput. Vis. 129, 3051–3068. https://doi.org/10.1007/s11263-021-01515-2.

Yuan, S., Li, L., Chen, H., Li, X., 2023. Surface defect detection of highly reflective leather based on dual-mask guided deep learning model. IEEE Trans. Instrum. Meas. https://doi.org/10.1109/TIM.2023.3310088.

Zhang, C., Liu, Y., Wang, K., Tian, J., 2023a. Specular highlight removal for endoscopic images using partial attention network. Phys. Med. Biol. 68, 225009. https://doi.org/10.1088/1361-6560/ad02d9.

Zhang, D., Liu, Y., Zhao, Y., Liang, J., Sun, B., Chu, S.J.A.S., 2023b. Algorithm Research on Detail and Contrast Enhancement of High Dynamic Infrared Images. 13, 12649. https://doi.org/10.3390/app132312649.

Zhang, T., Zhang, X., 2021. A novel algorithm for infrared image contrast enhancement based on neutrosophic sets. Quant. InfraRed Thermogr. J. 18, 344–356. https://doi.org/10.1080/17686733.2020.1786640.

Zhong, S., Fu, L., Zhang, F., 2023. Infrared image enhancement using convolutional neural networks for auto-driving. Appl. Sci. 13, 12581. https://doi.org/10.3390/app132312581.

Zhu, G., Chen, Y., Wang, X., Zhang, Y., 2024. MMFF-NET: multi-layer and multi-scale feature fusion network for low-light infrared image enhancement. Signal, Image Video Processing 18, 1089–1097. https://doi.org/10.1007/s11760-023-02797-4.

Zhu, Q., Zhang, Y., Li, Z., Yan, X., Guan, Q., Zhong, Y., Zhang, L., Li, D., 2021. Oil spill contextual and boundary-supervised detection network based on marine SAR images. IEEE Trans. Geosci. Remote Sens. 60, 1–10. https://doi.org/10.1109/TGRS.2021.3115492.

Zuo, C., Chen, Q., Liu, N., Ren, J., Sui, X., 2011. Display and detail enhancement for high-dynamic-range infrared images. Opt. Eng. 50, 127401–127409. https://doi.org/10.1117/1.3659698.